Title

Propagation of sound through a spicy ocean, the SOFAR overture

Journal

Journal of the Acoustical Society of America, 116(3)

ISSN

0001-4966

Authors

Dzieciuch, M

Munk, W

Rudnick, D L

Publication Date

2004-09-01

Peer reviewed

Propagation of sound through a spicy ocean, the SOFAR overture

Matthew Dzieciuch,[a] Walter Munk, and Daniel L. Rudnick
Scripps Institution of Oceanography, University of California at San Diego, La Jolla, California 92093

(Received 20 February 2003; accepted for publication 21 May 2004)

Using a closely sampled 1000-km hydrographic section in the eastern North Pacific, the sound-speed finestructure is separated into two component fields: (*i*) isopyncal tilt dominated by internal waves (the traditional view) and (*ii*) ''spicy'' (cold-fresh to hot-salty) millifronts associated with upper ocean stirring. Numerical transmission experiments show significant scatter within the mixed layer from the spicy fronts. This scattered energy arrives near the start of the SOFAR sequence, and is superimposed on a triplication of the channel dispersion at the transition from reflected to upper ocean refracted energy. (This SOFAR *overture* is totally different from the *finale* which has been prominent for over 50 years.) The critical dependence of the overture on mixed layer processes suggests a scheme for acoustically monitoring the upper oceans at surface-conjugate depths (3 to 5 km), offering some advantages over *in situ* monitoring. © *2004 Acoustical Society of America.* [DOI: 10.1121/1.1772397]

PACS numbers: 43.30.Re, 43.30.Qd [WJS] Pages: 1447–1462

I. INTRODUCTION

Perhaps the outstanding characteristic of long-range transmissions in the ocean is the high degree of variability. In the early days of SOFAR transmissions, attempts to account for the variability based on laboratory concepts of homogenous isotropic turbulence were favored for their analytical convenience. But ocean variability is neither homogenous nor isotropic. Munk and Zachariasen (1976) found such ''reliance on laboratory concepts...though fashionable, to be entirely misplaced,'' and then proposed, ''...internal waves and internal tides (as the) principal source of fluctuations.'' Their scattering estimates referred to (but did not include) ''intrusive and other forms of finestructure.''

For nearly 30 years internal waves have occupied a position near to monopoly in the literature on acoustic variability (Flatté *et al.*, 1979). But the consideration in this paper of frontal structure is not just a second item in an infinite menu of ocean variability; we suggest that the combination of internal waves and frontal activity can account for a major part of the measured variability.

Ewart *et al.* (1977) estimated the effect of non-internal-wave-related finestructure from data obtained in summer 1977 during the Mid-Ocean Acoustic Transmission Experiment (MATE) near Cobb Seamount in the northeastern Pacific. The temperature field was monitored from time series of moored sensors and vertical CTD profiles (Levine and Irish, 1981, 1986). The term ''finestructure'' was defined to represent a vertical structure in the temperature field with horizontal scales large compared to those of the internal waves (see also Garrett and Munk, 1971).

Ewart (1980) performed a numerical simulation of the effect of such finestructure on acoustic transmissions. Phases (travel times) remained unaffected but intensities were greatly modified. Here we examine acoustic transmissions through the ocean as measured by the towed vehicle SeaSoar. Ewart's vertical CTD finestructure profiles differ from the gradients measured with the SeaSoar horizontal tows in that many of the temperature ''jumps'' occur on scales small compared to the internal wave lengths. However, the spacing of fronts is comparable to internal wave scales, and spatial filtering does not readily separate the two fields. We perform the separation by a procedure that recognizes the intrinsic distinction between the two processes.

A cartoon (Fig. 1) will prepare the reader for the forthcoming analysis of ocean transects. The unperturbed ocean has a surface mixed layer with water of uniform density (as indicated by the density of dots) overlying a sharply increasing density structure $\rho(z)$. The isopycnals $z(\rho)$ are horizontal. Internal waves vertically displace the water particles, as indicated by the tilting isopycnals. However, the layers of constant density are not horizontally homogeneous: steep fronts separate regions of cold and fresh water (blue) from hot and salty water (red), with green indicating temperature and salinity averages of the blue and red waters, taken horizontally over many fronts. Temperature and salinity transitions are compensated, so that the density does not vary across the ''spice'' front. Accordingly the fronts do not play a role in ocean dynamics, but they do in ocean acoustics. Internal waves and spice fronts form two essential components of the sound-speed finestructure.

We have derived a scheme for separating the tilt and spice fields in a recent 1000-km section of temperature and salinity profiles in the North East Pacific. Numerical acoustic transmission experiments are conducted along (*i*) the measured profile, (*ii*) with spice removed, (*iii*) with tilt (internal waves) removed, and (*iv*) for the smoothed profile without any finestructure. The results are shown in the traditional timefront displays as they would be measured by a vertical receiver array at 1000 km range. Early timefronts are modified by the mixed layer processes, with different modification for different processes.

[a]Electronic mail: mad@ucsd.edu

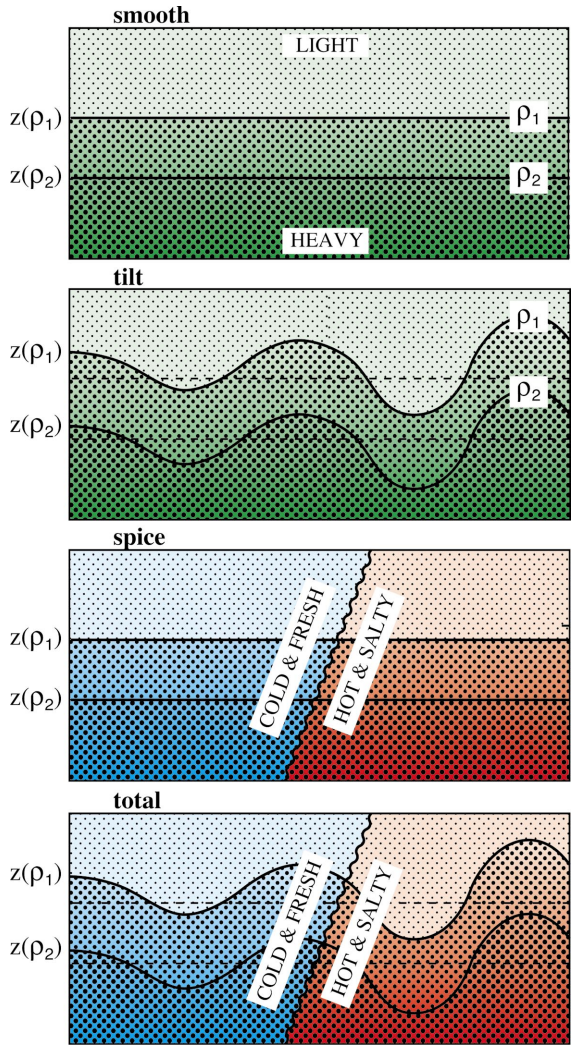

FIG. 1. Cartoon illustrating the separation of internal wave and spice related finestructure (see text).

To interpret the results, we consider a simple acoustic model which allows for (*i*) the early transition from surface reflected to upper ocean refracted rays, and (*ii*) the seasonal formation of the surface mixed layer. The resulting time-fronts are further modified by scattering within and beneath the mixed layer. The sensitive dependence of the overture on mixed layer processes suggests a scheme for acoustic monitoring; conducting the acoustic measurements at surface-conjugate[1] depths (3 to 5 km) has some advantages over *in situ* monitoring of upper ocean processes.

II. UPPER OCEAN FINESTRUCTURE

Figure 2 shows a potential density section in the upper 320 m of the North Pacific (Rudnick and Ferrari, 1999; Ferrari and Rudnick, 2000). Data were taken using a towed vehicle, SeaSoar, that is actively controlled from the ship by varying the pitch of its wings. A series of tows were done along 140 °W between 25° and 35 °N. First, SeaSoar was flown in a sawtooth pattern between 5 and 320 dbar, completing a cycle at least once per 12 min. A tow speed of 4 $\mathrm{m\,s^{-1}}$ produced a cycle in 2.88 km. Subsequent tows targeted surfaces identified in the first section. The second and third

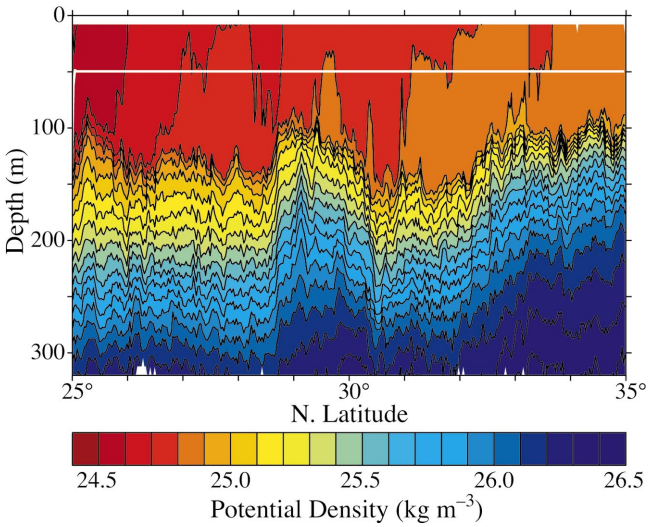

FIG. 2. Potential density in the upper ocean along 140 °W, measured using the towed vehicle SeaSoar (Rudnick and Ferrari, 1999). Contour interval is 0.1 $\mathrm{kg\,m^{-3}}$. Data are binned in depth and time prior to contouring, yielding a 3 km by 8 m resolution. Note the homogeneity of density in the upper mixed layer.

tows were along pressure surfaces in the mixed layer, 50 dbar, and in the thermocline, 200 dbar. It was found that the large-scale structure in the section were persistent over at least two weeks. Finescale features may change over the time required to complete the section, but the statistics should not, so the section offers a plausible realization of the finestructure.

A mixed layer of 100- to 150-m thickness lies atop the thermocline (Fig. 2). Density in the mixed layer is remarkably uniform, with differences between the surface and the bottom of the mixed layer of less than one part in 10^5. An outstanding feature in the mixed layer is the presence of fronts of all scales in which potential temperature and salinity transitions are density compensated (Fig. 3).

Fronts are common features of geophysical fluids, characterized by localized strong horizontal gradients in any of a variety of properties. Here, we are particularly interested in spice fronts, whose locally strong gradients are caused by the straining effects of stirring. As spice fronts have no density signature, these fronts have no effect on dynamics, but are ideal passive tracers. Young (1994) has given the interesting interpretation that the density compensation is a matter of survival: noncompensated fronts are gravitationally unstable and will slump; they are subsequently annihilated by the vertical mixing processes that form the upper homogenous layer. The surviving fronts are a manifestation of the stirring processes, which generate mean-square gradients. Little is known about the relevant time scales, but the dearth of finescale density fronts in the mixed layer suggests that the slumping process is fast relative to the processes (surface flux and vertical entrainment) that cause density anomalies.

The familiar horizontal variations of sound-speed caused by internal waves are associated with the prominent undulations of isopycnal contours beneath the mixed layer (Fig. 2). Less familiar are the transitions associated with the temperature and salinity fronts in and beneath the mixed layer. These frontal transitions are very different from the Gaussian-like

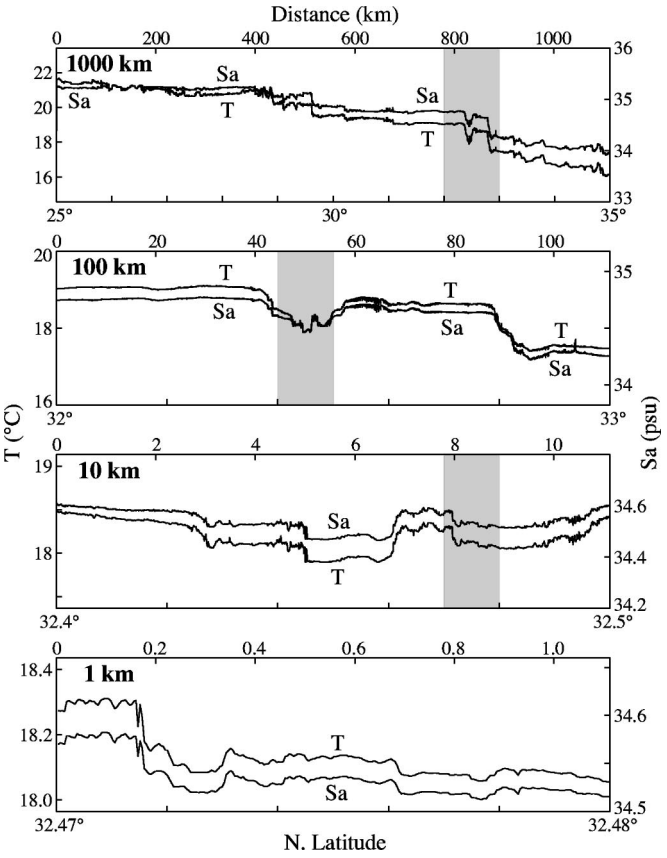

FIG. 3. Potential temperature (blue) and salinity (green) along 50 dbar (white line in Fig. 2). Vertical axes are so scaled that equal excursions of temperature and salinity imply equal but opposite effects on density. The upper panel covers the entire tow; succeeding panels are magnified by a factor of 10 of the shaded region of the panel above.

variability associated with internal waves. Although the temperature T and salinity Sa transitions are compensated with regard to density, this does not imply that the sound-speed is horizontally uniform; in fact the parameters that are density compensating are sound-speed enhancing. It is useful to define the field orthogonal to the density field in a T/Sa diagram (Fig. 4). This is called spice as it varies from cold and fresh to hot and salty.[2] Munk (1981) used the term spice to distinguish density-compensated ''globs'' from internal wave-related finestructure. Let

$$\frac{\Delta C}{C}=a\Delta T+b\Delta Sa, \quad \frac{\Delta\rho}{\rho}=-\alpha\Delta T+\beta\Delta Sa,$$

$$\frac{\Delta\mu}{\rho}=\beta\Delta T+\alpha\Delta Sa \tag{1}$$

for the variation in potential sound-speed, density, and spice as functions of potential temperature and salinity. Typical numerical values are

$$a=2.0\times10^{-3}\ ^\circ\mathrm{C}^{-1}, \quad \alpha=0.25\times10^{-3}\ ^\circ\mathrm{C}^{-1},$$

$$b=0.74\times10^{-3}\ \mathrm{PSU}^{-1}, \quad \beta=0.75\times10^{-3}\ \mathrm{PSU}^{-1},$$

where °C and PSU are temperature and salinity units. Write

$$\frac{\Delta C}{C}=a\Delta T(1+m), \quad \frac{\Delta\rho}{\rho}=-\alpha\Delta T(1+n) \tag{2}$$

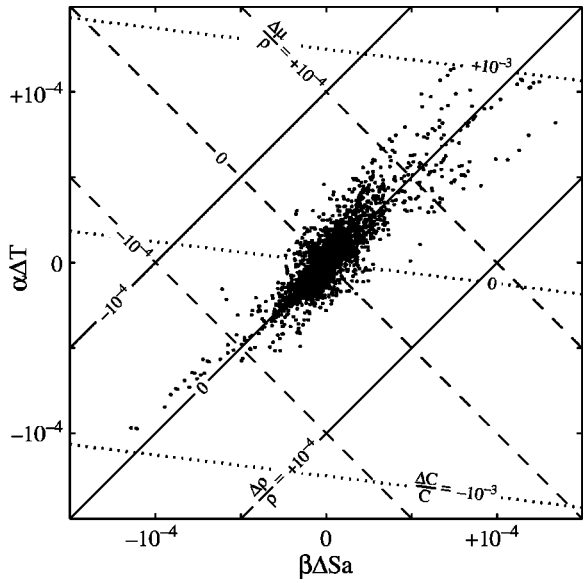

FIG. 4. A scatter plot of $\alpha\Delta T$ versus $\beta\Delta Sa$ throughout the mixed layer (Fig. 1). Points are horizontal differences over the resolution length of 2.88 km. Three sets of contour lines are drawn according to Eq. (1); density (ρ) and spice (μ) contours have slopes $R=\pm1$ (by definition). Data align along $\Delta\rho/\rho=0$, indicating that temperature and salinity differences are compensating in their effect on density. $\Delta C/C$ contours have a slope of -0.12 (see text).

so that

$$m=\frac{-\alpha b}{a\beta}n=-0.12n. \tag{3}$$

Total compensation corresponds to a ''density ratio''[3] of $n=\beta\Delta Sa/(-\alpha\Delta T)=-1$ and $m=+0.12$. Accordingly, in the spicy fronts of the upper North Pacific, the frontal salinity transitions lead to a near 100% *reduction* in the temperature-associated density transitions, and a 12% *augmentation* in the temperature-associated sound-speed transitions.

Beneath the mixed layer the temperature effects dominate, with the density ratio diminishing abruptly from $n=-1$ to nearly $n=-\frac{1}{2}$, a curiosity related by Schmitt (1981, 1994) to salt fingering (see also Stommel, 1993; Rudnick and Martin, 2002). Regardless of the numerical values, in a spicy environment with temperature fronts the density transitions are greatly reduced but the sound-speed transitions are somewhat enhanced by the salinity transitions.

Figure 5 shows sound-speed variability along constant density surfaces. This is equivalent to displaying sound-speed in an ocean without internal waves.

A. Separation into tilt- and spice-related processes

We are quite accustomed to filtering in space and time. But here we have two processes, internal waves and spicy fronts, with overlapping scales. For separation we depend on the intrinsic distinction between the two processes.

By mapping and filtering the recorded temperature and salinity fields in density space, we can separate processes that cause spice variability, such as stirring, from those associated with isopycnal displacement, such as internal waves. Oceanographers would stop there, but acousticians require these filtered fields in physical space be appropriate to sound

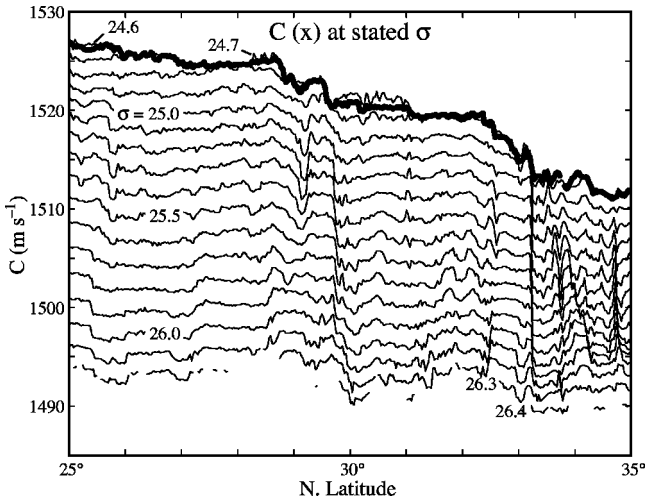

FIG. 5. Sound-speed profiles along constant potential density surface by steps of 0.1 kg m^{-3}. Shorter curves at the top are from outcropping isopycnals; discontinuous curves at the bottom extend below the deepest observations. The heavy purple line near the top is from a tow at near the middle of the mixed layer.

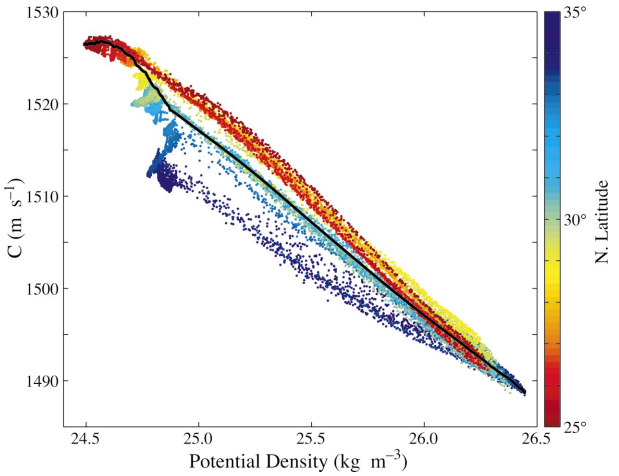

FIG. 6. Scatter plot of sound-speed against potential density for the upper ocean. The relation varies with latitude; the black curve is the latitude-averaged sound-speed.

transmission. Let $T(x,z)$ and $\rho(x,z)$ designate the measured fields of potential temperature and density measured as a function of latitude and depth. We replace the independent depth variable with potential density in the expression for temperature, yielding $T(x,\rho)$. Similarly, we can obtain $Sa(x,\rho)$ and hence $C(x,\rho)$; any contribution from internal waves and other tilt-generating processes is eliminated in the x, ρ-display. To return to physical space, we place the ρ-coordinate at the position of its average depth (Fig. 1, spice panel). The ''spice'' ocean can be imagined as the straightening-out of isopycnals by pulling them horizontally.

The ''tilt'' ocean is obtained by computing the x-average, holding ρ constant, $T_{\text{tilt}}(\rho)=\langle T(x;\rho)\rangle_x$, and mapping back into physical space by using

$$T_{\text{tilt}}(x,z)=T_{\text{tilt}}(\rho(x,z)) \tag{4}$$

and similarly for $Sa_{\text{tilt}}(x,z)$ and $C_{\text{tilt}}(x,z)$.

The cartoon in Fig. 1 neglects some essential considerations: we do not wish to throw out permanent oceanographic features with the elimination of internal waves. This is accomplished as follows: the measured field $\rho(x,z)$ is inverted to yield the isopycnals $z(x;\rho)$. Next, the isopycnals are operated on by a low-pass filter LP (Hanning filter with 50 km horizontal scale) yielding a ''regional mean depth''

$$z_{\text{LP}}(x;\rho)=\text{LP}[z(x;\rho)], \tag{5}$$

and its inverse $\rho_{\text{LP}}(x,z)=z_{\text{LP}}^{-1}(x,\rho)$. The spice contribution is then obtained from

$$T_{\text{spice}}(x,z)=T(x;\rho_{\text{LP}}(x,z)). \tag{6}$$

This eliminates internal waves while retaining large-scale hydrography. Transient nearly geostrophically balanced motions, often called mesoscale eddies, are a dominant source of variability at length scales of tens of kilometers. Mesoscale eddies cause isopycnals to tilt, and stir spice gradients. As such, they contribute to both the tilt and spice fields.

Finally, we require an ocean with smooth isopycnals and no spice. This is accomplished by mapping the horizontally averaged temperature back into physical space using the low-passed density field:

$$T_{\text{smooth}}(x,z)=T_{\text{tilt}}(\rho_{\text{LP}}(x,z)). \tag{7}$$

This spice-free ocean, containing only large-scale isopycnal tilt, is a reference against which to evaluate the effect of spice and internal waves. The transformation between density space and physical space is nonlinear, and so the total field of any variable cannot be a sum of the smooth, spice, and tilt fields. For a meaningful analysis all sound-speed fields must have a sound channel.

Figure 6 is a scatter plot for the entire section. This functional relationship $C(\rho)$, indicated by the black line, between sound and potential density follows the center of mass (measured in the vertical) of the points in the scatter plot. The vertical scatter is a direct consequence of spice. The white spaces between points are caused by spice fronts (for example, 25 kg m^{-3} at 31 °N). Our examinations of the tilt field, and previous studies that ignore spice, essentially use a characterization of sound-speed that is a function only of density, equivalent to the black line. The scatter plot shows the sound-speed variability lost in such a characterization.

Figures 7 and 8 show the contributions of tilt and spice to the upper ocean fields of salinity and sound-speed. The bottom panel shows the total fields, as directly measured using SeaSoar. By construction, contours in the tilt-only sound field parallel the isopycnals in Fig. 2; in particular, the spice variations in the northern mixed layer are absent. The spice field is superimposed on smooth isopycnals. A careful comparison of the total and spice fields reveals the spice fronts in the total sound-speed. A smooth sound-speed field where the only variations are due to large-scale tilt is shown in the top panel. This is our approximation to an ocean with no internal waves and no spice. The smoothed profile contains the large-scale ocean variability along this 25 °N to 35 °N ocean section.

Strong, vertically coherent spice fronts can be seen near 29° and 33 °N (Fig. 3). These fronts are likely permanent

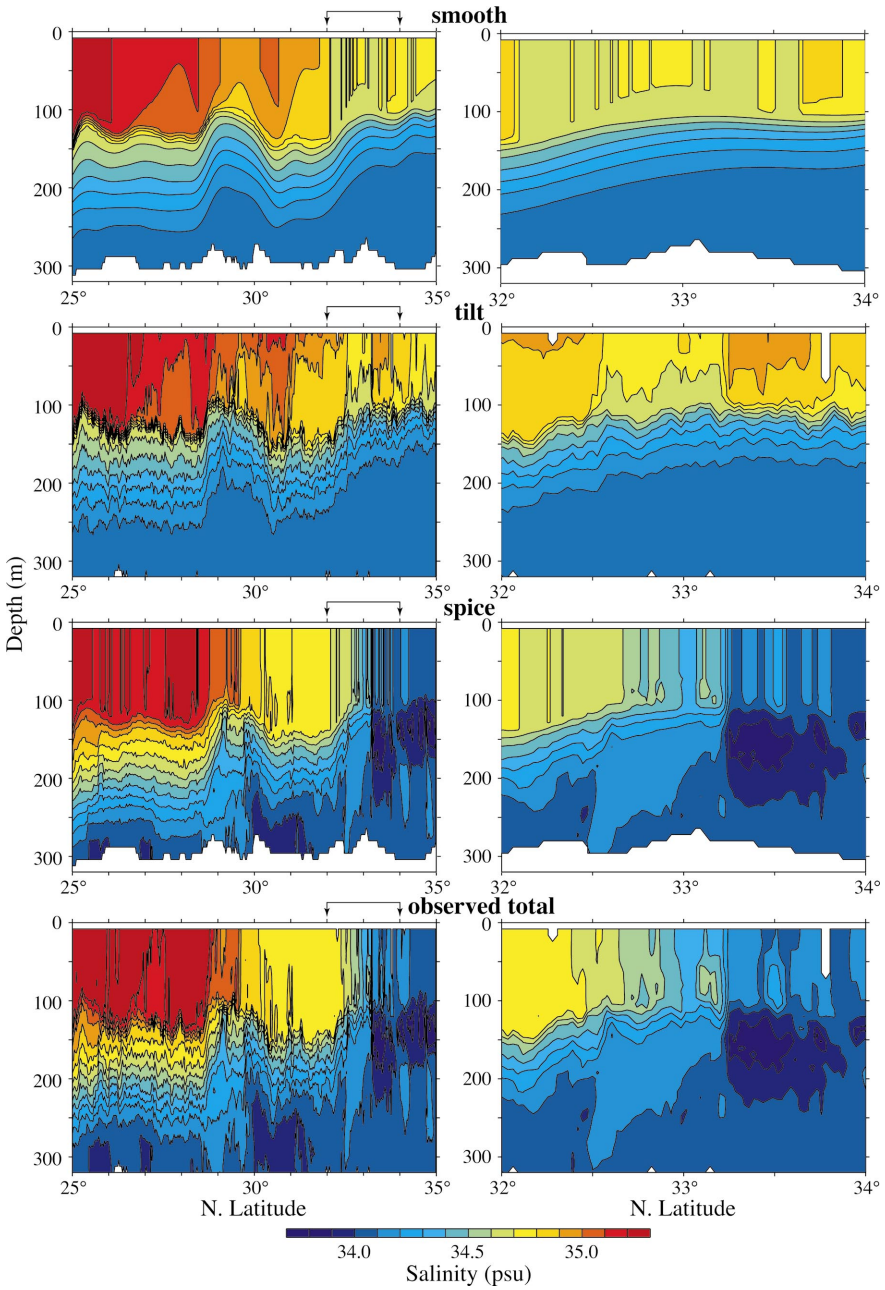

FIG. 7. Fields of salinity with 0.1 psu contour intervals for the entire section (left) and a subsection (right).

features of the region (Yuan and Talley, 1992), although their exact positions may vary. There are also variations of relatively short vertical scale, as for example, near 32 °N and 1505 m s^{-1}. This small vertical scale variability changes significantly between successive occupations of the section several days apart.

In the thoroughly mixed upper layer the sound-speed perturbations associated with internal-wave-induced vertical displacements are small, and the effect of spice fronts dominates. In the mixed layer at 48 m, $\Delta C = 0.24$ m/s for the rms difference at the resolved 3-km spacing. Beneath the mixed layer at 200 m we find $\Delta C = 0.74$ m/s and 0.35 m/s associated with internal waves and spice, respectively. For comparison, the pronounced frontal feature at 29 °N has differences of order 0.5 m/s per 3 km. A mean slowing by -0.1 m/s in 3 km is associated with the south-to-north cooling along the 1000 km profile. The statistical distribution of the horizontal gradients associated with isopycnal tilting are nearly Gaussian (as has long been known), whereas the frontallike distribution of spice leads to large departures from a Gaussian distribution.

B. Patching the upper ocean to Levitus climatology

We have patched Levitus February climatology (Levitus, 1994; Levitus *et al.*, 1994) to the upper 320-m section taken by SeaSoar 23 January–20 February 1997 (Fig. 9). There is no good way of splicing a single section to a decadal climatology. After many tries we have settled on a least-square vertical cubic spline applied separately to the temperature and salinity fields, and subsequently converted to sound-speed. The cubic spline allows for the disparate error bars,

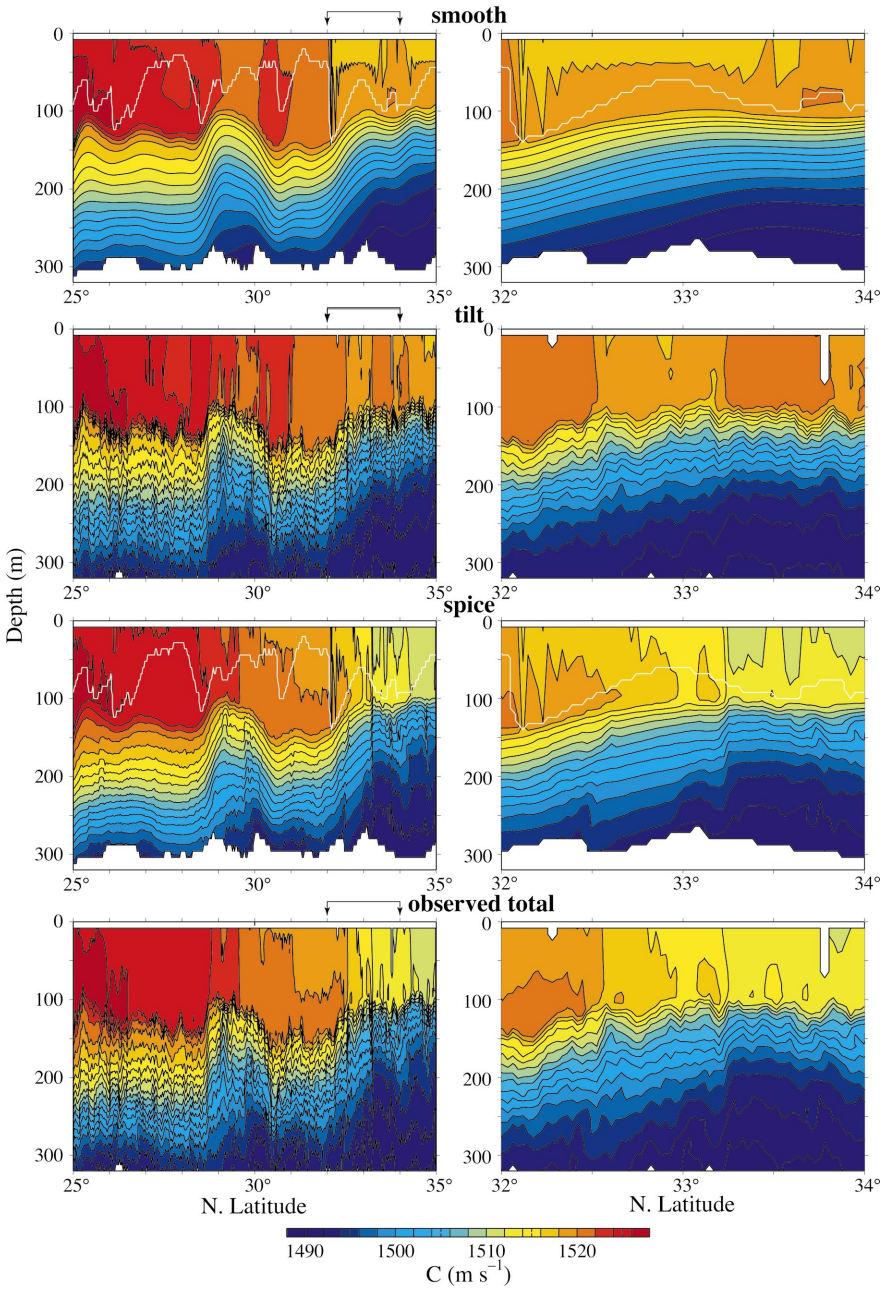

FIG. 8. Fields of sound speed with 2 m s^{-1} contour intervals for the entire section (left) and a subsection (right). Left bottom panel is the observed field (shown in Fig. 2). See text for separation into tilt-only, spice-only, and smoothed (no tilt, no spice) fields. The fields serve as basis for the following numerical transmission experiments. The white line indicates the region above which fields are determined by extrapolation to the surface as described in the text.

0.001 °C, 0.001 PSU for SeaSoar and 0.1 °C, 0.1 PSU for the climatology. Since the sampling grid of the two data sets are different, care has to be taken to avoid having the spline impose excessive curvature on the interpolated profile. The adopted procedure is to relax the SeaSoar error bars at the two deepest grid points (312 m, 320 m) by a factor of 100 to match the climatology error bars. This method avoids dC/dz discontinuities with resulting acoustic caustics.

The climatological mean field suppresses the internal wave perturbations and all but the major permanent frontal features. Horizontal surveying of the deep ocean is difficult, and we know little about the deep spice structure. However, spice heterogeneity is known to decay with depth (Ferrari and Rudnick, 2000), and so we suspect that spicy fronts are features mainly of the upper oceans. On the other hand, internal waves are known to pervade the entire water column, and their neglect here must lead to an underestimate in the scattering.

III. A NUMERICAL EXPERIMENT IN ACOUSTIC SCATTER

In order to investigate the effects of small-scale structure on acoustic propagation, we devised a series of numerical experiments resembling typical field experiments see Colosi (1999), (Fig. 10). A broadband sound source at 100±12.5 Hz was placed on the sound channel axis (730 m) at 25 °N. Sound pressure as function of time and depth was calculated

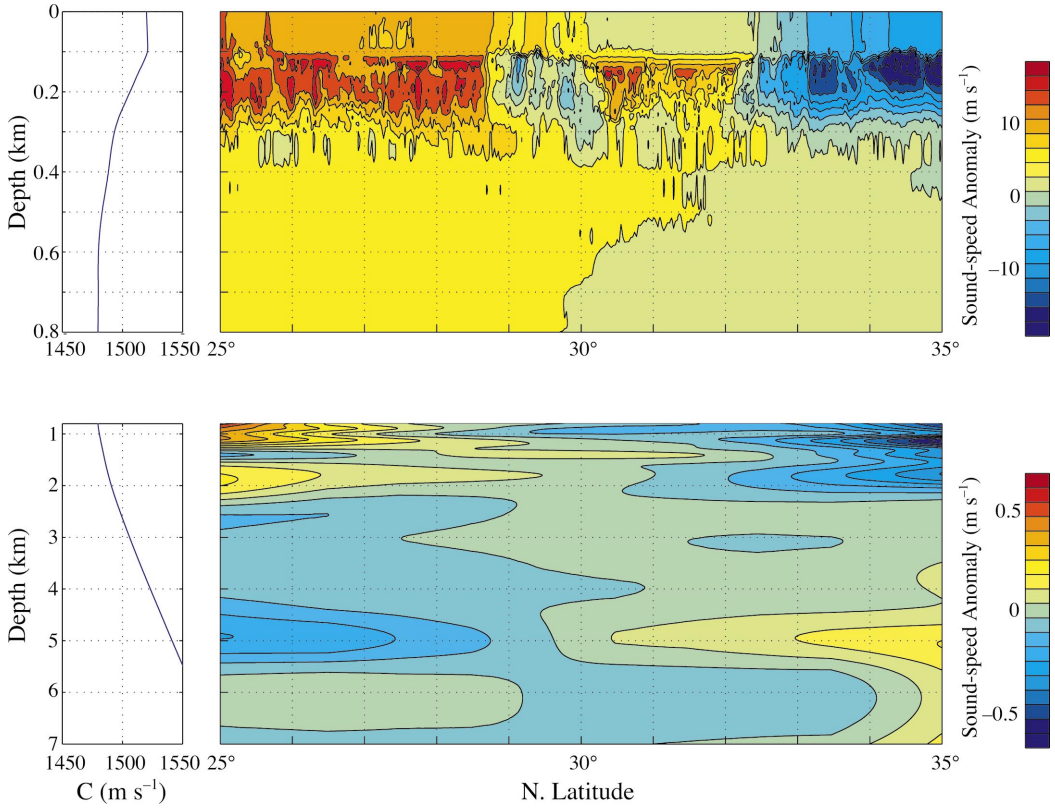

FIG. 9. Contours of sound-speed anomalies relative to mean profile (left panels). Measurements from SeaSoar tows in the upper 300 m are patched to the Levitus Ocean Atlas climatology. Note the intensive sound-speed finestructure in the upper layers, in contrast to the almost uniform potential density (Fig. 2).

at a range of 1000 km for each of the four ocean realizations described in the previous section. A further calculation was performed for the range-averaged smoothed profile.

A. Parabolic equations

The standard parabolic equation (PE) method was applied to underwater acoustics by Tappert (1977), but the split-step Pade PE (Collins, 1989), available in a computer code called RAM, served as a basis for all numerical experiments since deep-water profiles with a mixed layer channel require PE methods that handle wide propagation angles.

The range-averaged profile in the left panel of Fig. 9, with a mixed layer in the upper few hundred meters, is an essential feature in the scattering process (as we shall see). A grid spacing of 0.2 m in the vertical, 50 m in range, with four Pade terms, was found to converge and the result is shown in the top panel of Fig. 10. We are concerned with water-borne energy, and so placed a thick absorbing layer beneath the water column at 5-km depth to trap any energy that might interact with the bottom and obscure the mixed layer arrivals. In the range-independent case of the top panel, a comparison with an accurate mode computation by the Chebyshev method (Dzieciuch, 1993) was made and the mismatch was too small to be visible. Ray codes also matched the travel time predicted by the RAM PE and the modal calculation, except for the earliest arrivals which have turning depths just below the surface and thus finite-frequency boundary effects are important. It is interesting that the range-averaged case shows more early structure than the range-dependent cases.

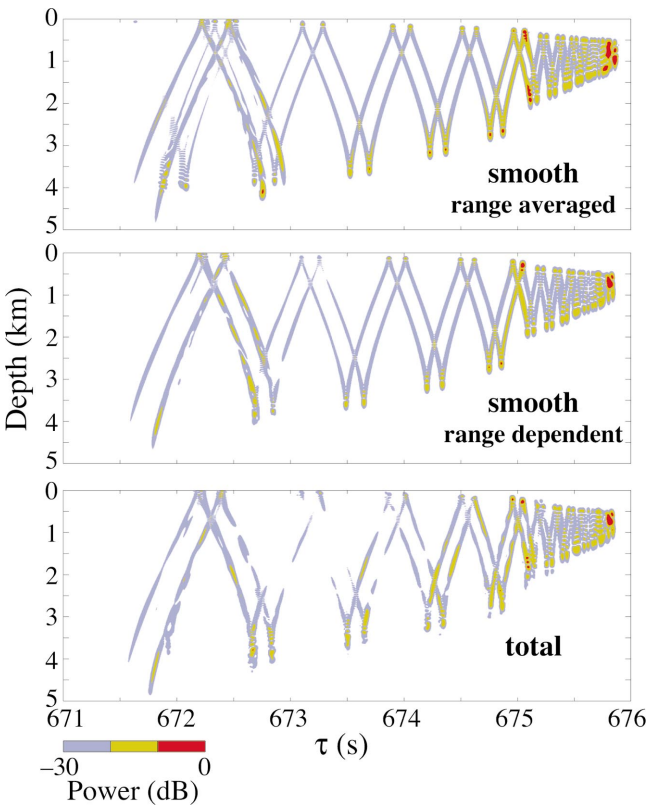

FIG. 10. Intensity field for an acoustic transmission from an axial source at 25 °N to a receiving array at 35 °N. The upper panel corresponds to the range-averaged sound-speed profile (Fig. 9, left). The second and third panels are for transmission through the smooth and observed fields of Fig. 8. All contours are relative to the axial climax in the smooth range-dependent transmission.

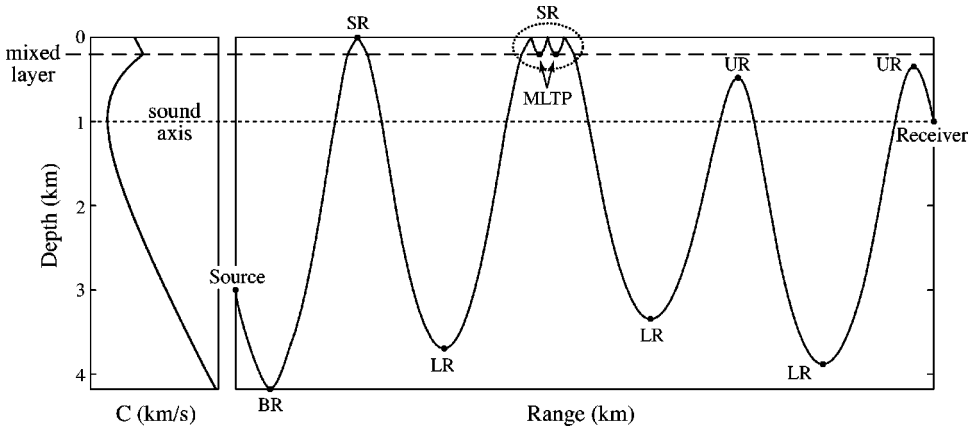

FIG. 11. Definition plot. UTP=SR+UR=2+2 refers to the number of upper turning points, consisting of SR (surface reflected) and UR (upper refracted) turning points. Similarly LTP=BR+LR=1+3 is the number of lower turning points. MLTP=2 is the number of lower turning points in the mixed layer; one or more trapped mixed layer loops counts as a single SR (see figure). For the above ray path, Id: −(UTP+LTP)=−8, %SR=100 SR/UTP=50%, %ML=100 MLTP/(MLTP+LTP)=33%, %BR=100 BR/LTP=25%.

B. Timefronts from an axial source

Figure 10 shows the computed intensity contours for transmission through the total measured field of sound-speed and a smoothed (no spice, no tilt) field (see Figs. 8 and 9). Intensities (down to −30 dB) refer to same maximum in the finale of the center panel. The top panel corresponds to a range-averaged profile of the smoothed field. All the numerical experiments yield the now familiar accordionlike timefronts (Munk and Wunsch, 1979, Fig. 4). The range-averaged field does not differ dramatically from the smooth range-dependent field in spite of the significant latitudinal change in the upper layers along the transmission path. Scattering from finestructure leads to some added complexity in the early arrival pattern. Using the climatological (rather than measured) deep ocean leaves the late arrivals unscattered, unlike the measured pattern of long-range transmissions (Colosi *et al.*, 1994).

We can recognize three distinct phases:

(*i*) the final half second of unresolved arrivals of increasing intensity leading to the abrupt cutoff (the classical SOFAR finale),

(*ii*) the central two seconds of resolved reflected and refracted arrivals which form the basis of tomographic inversions, and

(*iii*) the leading second of steep surface-reflected arrivals with fractured fronts and sensitivity to scattering.

Our emphasis will be on the SOFAR overture, from the earliest arrivals to the transition from reflected to refracted energy. This phase is particularly sensitive to the upper ocean processes under consideration here. For that purpose all subsequent results will be for a source at 3 km which places later arrivals (with turning points beneath 200 m) into a geometric shadow. The ray designations SR, UR, LR,... for surface reflected, upper refracted, lower refracted,... (an unsatisfactory compromise with traditional designations) are defined in Fig. 11. Upper turning points can be surface reflected or refracted, UTP=SR+UR; similarly LTP=BR+LR.

C. Abyssal source

Figure 12 illustrates the principal results of this paper. The four panels in Fig. 12(a) give the intensity fields corresponding to the four sound-speed fields in Fig. 8. The tilt-related scatter does not contribute to the penetration into the mixed layer. The principal effect is to extend the latest timefront into the acoustic shadow and to increase the turning sound-speed, resulting in a somewhat deeper lower turning point and a slightly higher upper turning point. (We remind the reader that internal wave scatter is here restricted to the upper 320 m.)

Spice enhances the intensity of the leading two fractured timefronts, and raises the two upper turning points at 673.5 s from beneath the mixed layer to the surface (see Fig. 13). This sharp modification in turning elevation of the −38 timefront is not accompanied by a significant change in turning sound-speed; accordingly, there is no appreciable lowering of the lower turning point at 674.0 s. However, the preceding SR timefront −36 is lowered from 3.7 to 3.9 km.

The question immediately arises as to the identification of the modified timefronts. Here we resort to the classical method of ray construction (4888 rays were launched at 5 millidegree intervals) with ray arrivals at the receiving array indicated by dots in Fig. 12(b); for comparison, the PE intensities above −30 dB are indicated by the underlying gray bands. Identification follows MWW nomenclature;[4] for example, +35 indicates a upward launch angle with 18 upper and 17 lower turning points. The distance between dots is an indication of intensity (often the dots are so closely spaced as to appear as a line).

We ignore internal reflections; a sharp interface reflects significant energy for glancing incidence at angles less than $\sqrt{\Delta C/C}$. At the bottom of the mixed layers, ΔC of order 1 m/s can occur within a few meters of depth. Yet the agreement between the PE-derived and ray-derived timefronts is generally satisfactory.

In the smooth ocean, the earliest[5] recorded timefront, −33a, is a weak arrival with only 136 rays (2.8%), each consisting of 16 upper and 17 lower turning points. For the

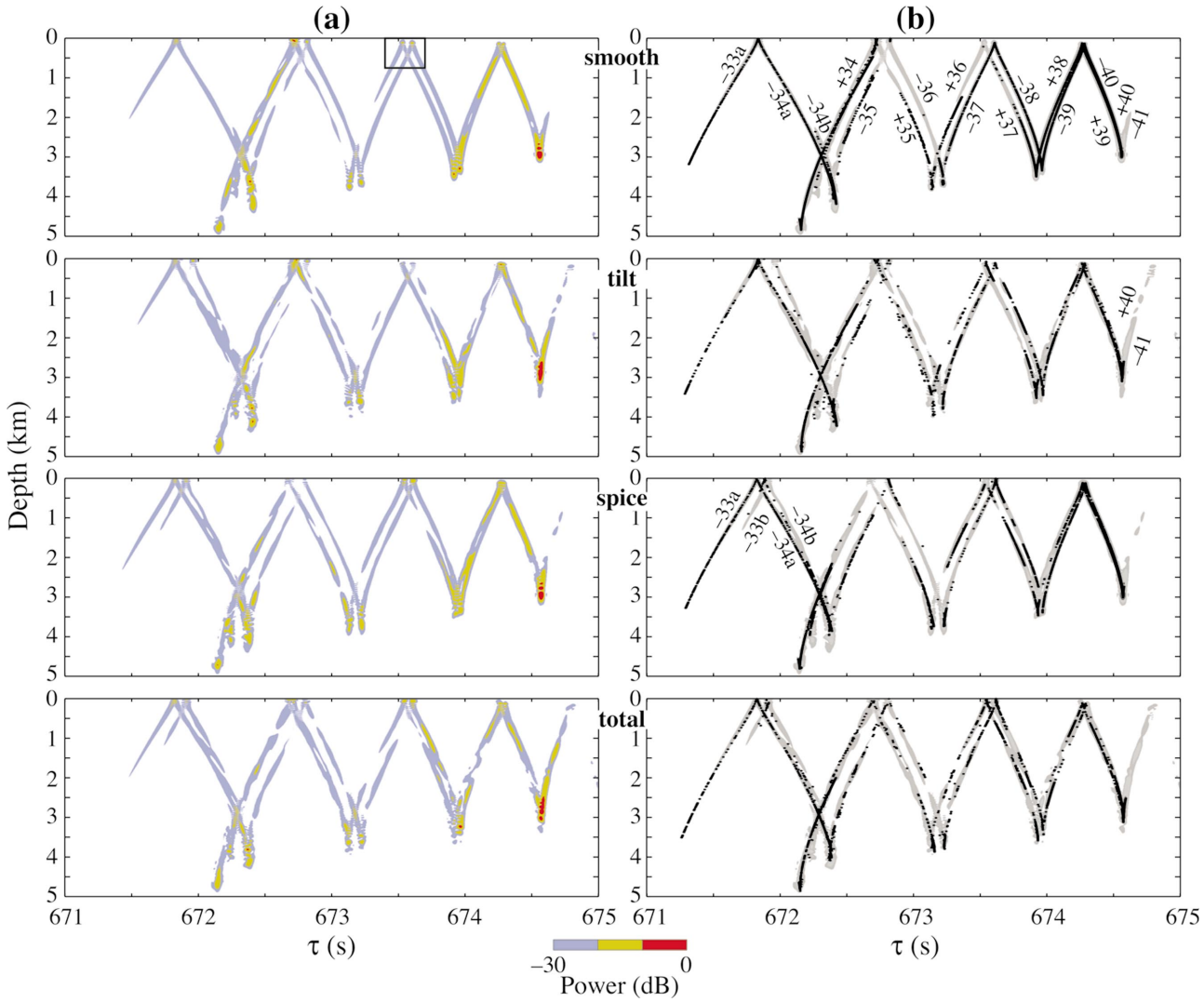

FIG. 12. (a) Computed PE intensity contours relative to the late ''smooth'' arrival from an abyssal source (3 km depth, conjugate to 200 m) at 25 °N to a receiving array at 35 °N for the smooth, spice, tilt (mostly internal waves), and total observed sound-speed profiles in Figs. 8 and 9. An enlarged version of the field within the rectangle is shown in Fig. 13. (b) Dots designate time and depth of ray arrivals at the receiver range, with PE intensities above −30 dB shaded. The ray designator −35 (for example) implies a negative launch angle with 17 upper and 18 lower turning points.

combined 136 rays along the −33a timefront, UTP=136 ×16=2176; all are surface reflected. Of the LTP=136×17 =2312 lower turning points, only 7 (0.3%) are bottom reflected. In the spicy ocean this is followed in 80 ms by a second arrival, −33b, with the same ray identifier −33. The two arrivals have dramatically different turning depths, 4.8 versus 3.9 km. The spicy rays have 5.6% of loops trapped in the mixed layer. The −33b arrivals are extremely weak in the tilt-only ocean.

The transition from surface reflected to upper refracted is abrupt for a smooth range-independent ocean; tilt and spice both extend the time of surface reflections. Rays trapped in the mixed layer are a feature of the transition; they are absent in the earliest and later arrivals.

With regard to the trailing timefronts +40 and −41, we note that the ray arrivals are concentrated at the lower turning points. The extension of intensity (without rays) into the upper ocean must be associated with diffraction. The prominent role by tilt is not understood. Finescale structure in the deep ocean (here neglected) would further extend the trailing timefronts (Colosi, private communication, 2003).

IV. A MODEL FOR THE SOFAR OVERTURE

We wish to interpret the results of the numerical experiment; in particular, the early arrival structure is very complex and sensitive to the formation of mixed layers. Here we look to an analytical model for guidance. The *temperate* profile (also known as the *canonical* profile; see MWW 2.18) is the simplest (but not a simple) representation of the sound channel at temperate latitudes. A global compilation of sound-speed profiles (MWW, Appendix B) exhibits a wide degree of variability, yet the temperate profile provides a rough description for conditions in the central North Pacific. The model is range independent; the resemblance of the upper two panels in Fig. 10 suggests that the principal features of the arrival pattern are retained in a range-averaged representation.

A convenient starting point is the *action variable* (Wunsch, 1987; Brekhovskikh and Lysanov, 1982; MWW, 2.5)

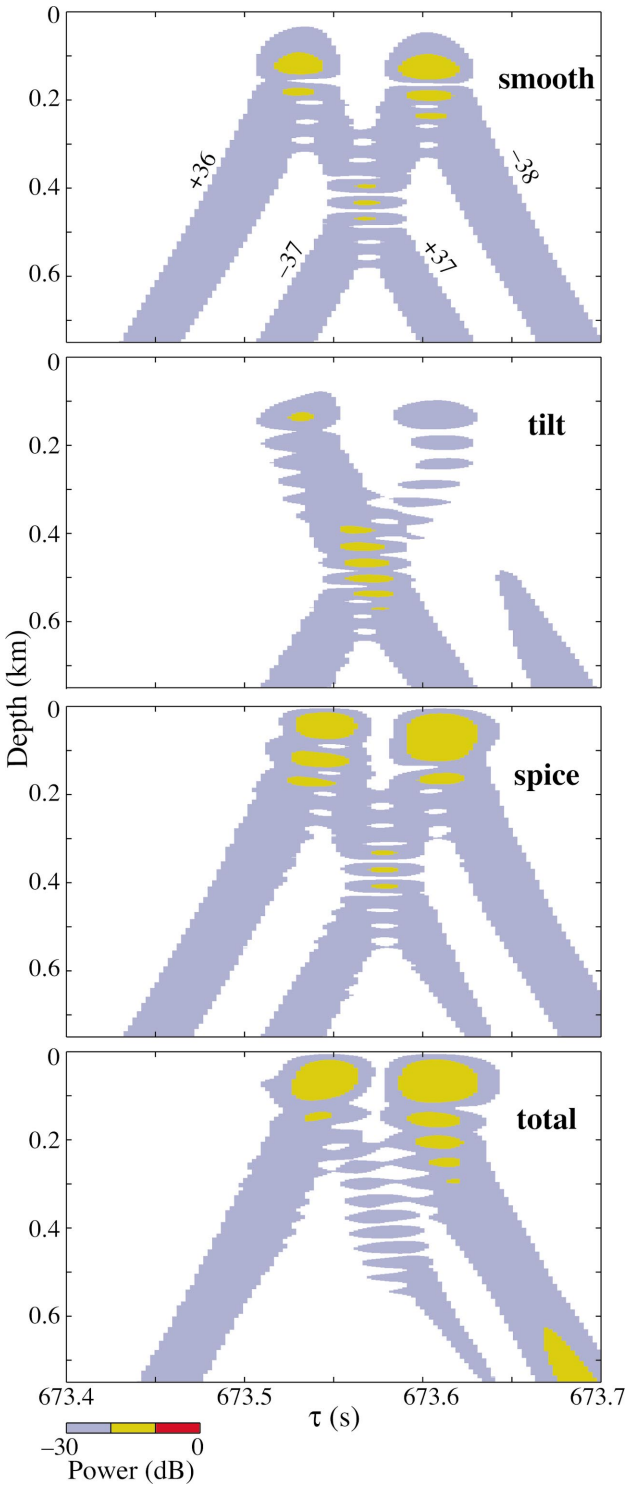

FIG. 13. An enlarged view of the intensity field near the surface within the rectangle in Fig. 12.

$$A(\tilde{S}) = 2\int_{\tilde{z}^-}^{\tilde{z}^+} dz (S^2 - \tilde{S}^2)^{1/2}, \tag{8}$$

where $S(z) = 1/C(z)$ is the sound *slowness*, and $\tilde{S}$ is the slowness at the turning depths $\tilde{z}^{\pm}$. Range and period of a ray loop are conveniently given in terms of the action and its derivative $A' \equiv dA/d\tilde{S}$:

$$R = -A', \quad T = A + R\tilde{S}, \tag{9}$$

with group-slowness and phase-slowness

$$s_{gr} = T/R = \tilde{S} - A/A', \quad s_{ph} = \tilde{S}. \tag{10}$$

The topology of the transition from refraction to surface-reflection is determined by the combined action $A(\tilde{S})$ (Fig. 14) in the sound channel plus the overlying mixed layer (see the Appendix for the cumbersome details). We choose phase versus group slowness for a representation of the dispersion (Fig. 15). The ordinate s_{gr} is readily interpretable as the traveltime $\tau = r s_{gr}$ (from 664 to 667 s); the abscissa $s_{ph} = S(\tilde{z}) \equiv \tilde{S}$ is a measure of turning depths $\tilde{z}^{\pm}$ above and beneath the axis. Alternately, going back to Snell's law, $\tilde{S} = S_{AX} \cos \theta_{AX}$ is a measure of the ray inclination at the axis.

We start with the case of no mixed layer (Fig. 15). Point **A** refers to the axial finale with $s_{ph} = s_{gr} = S_{AX}$. Preceding (refracted) arrivals of increasing steepness are of lower phase-slowness (increasing separation of turning depths from the axis). The dispersion follows a smooth curve up to point **B** where the upper refracted turning point reaches the surface. Steeper rays are surface reflected and of increasing group-slowness until **C** when the situation once again reverses. For arrival times between 665.3 and 665.7 s there are three branches (Fig. 15, top), and this triplication of arrivals accounts for the complexity of the early timefronts. Bottom interactions may cause further modifications (see Fig. 15, top, for the 5-km depth); it is an accident of nature (depending as it does on the temperature profiles and depths of the world oceans) that this interaction occurs in the vicinity of the triplication.

We can interpret the triplication in the terms of the properties of the temperate action profile. Normal dispersion means that steeper rays (smaller $\tilde{S} = s_{ph}$) travel faster (smaller s_{gr}). A transition between normal and abnormal dispersion infers that [using Eq. (10)]

$$s'_{gr} = 1 - \frac{(A')^2 - AA''}{(A')^2} = \frac{AA''}{(A')^2} = 0 \tag{11}$$

or $A'' = 0$, the definition of a caustic. The range of a double-loop is the sum of an upper and lower loop range: $R = R^+ + R^-$. Going from **A** to **B** in the direction of *decreasing* $\tilde{S}$, the loop range *increases* $[dR/d(-\tilde{S}) \equiv -R' = +A'' > 0]$; for the temperate model R increases from 42 km at **A** to a maximum of 53 km at **B**. In this interval the increase of R^- dominates over the decrease of R^+ (the normal situation). At point **B** the upper loop changes from refracted to surface-reflected, followed by a sharp decrease in R^+ dominating the total range R which reaches a minimum at **C**. With further steepening the contribution of the shrinking upper loop to the double-loop range becomes increasingly irrelevant and the lengthening lower loop dominates, restoring normal dispersion. Timefronts at a fixed range and fixed time determine the dispersion at discrete points which may or may not resolve the triplication.

The situation is similar for mixed layers (Fig. 15), with one important difference: a discontinuous decrease in group-slowness when the upper turning point reaches the lower boundary of the mixed layer.

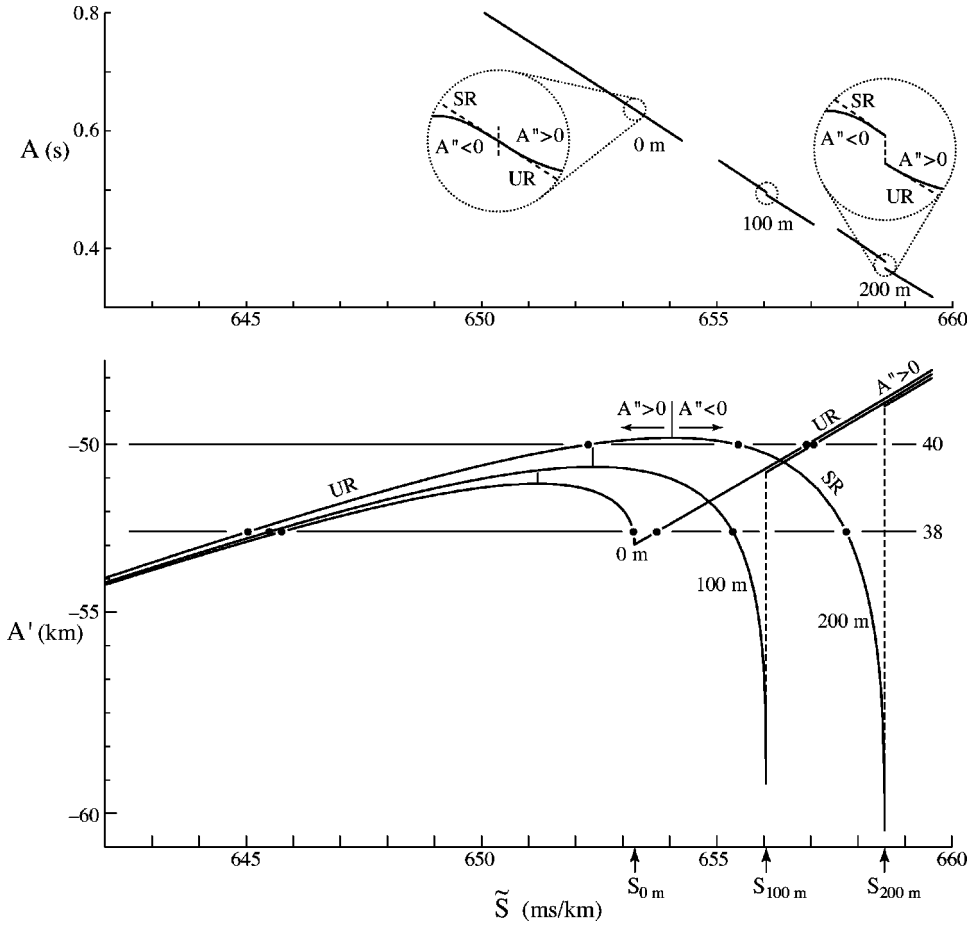

FIG. 14. The action variable A and its derivative $A' = dA/d\tilde{S}$ for the transition from refracted (UR) to surface reflected (SR) propagation, with mixed layer depths of 0, 100 and 200 m, respectively. A and A' are continuous for the case of no mixed layer, and discontinuous otherwise; in all cases A'' changes discontinuously from positive to negative as the ray path changes from UR to SR, and then back to positive (left of the peaks), with profound implications to the arrival structure. Dots indicate eigenrays 38 and 40.

V. THREE FEATURES OF INTEREST

The concentration of energy along the discrete timefronts, a consequence of Fermat's principle, is well known but nonetheless noteworthy: more than 95% of τ, z-space (Fig. 12) is at less than the -30 dB level, and more than 95% of the emitted rays are concentrated along the timefronts. Scattering processes lead to only a slight broadening of the timefronts, and to a slight bias (to be treated in a separate paper).

A further concentration is achieved by subjecting the timefronts to the turning-point filter TPF (Dzieciuch *et al.*, 2001):

$$P(\theta_{AX}, \tau_{AX}) = \sum_i \left[p_i(\tau_{AX} + \Delta\tau(z_i, \theta_{AX})\right], \tag{12}$$

where

$$\Delta\tau(z_i, \theta_{AX}) = \int_{z_A}^{z_i} dz \sqrt{S^2(z) - S_A^2 \cos^2 \theta_{AX}} \tag{13}$$

is the time delay relative to the axial arrival τ_{AX} for a receiver at elevation z_i, assuming an axial inclination θ_{AX}. [At constant slowness this reduces to the linear beamformer $\Delta\tau = (z_i - z_{AX}) S \sin\theta$.] The filtered intensity is plotted in s_{ph}, s_{gr}-space, with $s_{ph} = S_{AX} \cos\theta_{AX}$ and $s_{gr} = \tau_{AX}/r$ (Fig. 16). This is our preferred space for the acoustic monitoring of ocean processes.

There are many features to be accounted for. We shall consider three features in particular; they appear in all presentations but are highlighted in the three boxes of the TPF outputs.

Diffraction. Late refracted arrivals $+40$, -41 have PE intensities but no associated rays beyond the lower turning point (Figs. 12(a) and (b)]. The feature is more prominent at 50 Hz than at 200 Hz, as one would expect. All this is consistent with diffraction into the geometric shadow. In the real ocean with deep finestructure the late scattered arrivals are even further extended (Dushaw *et al.*, 1999), but the high intensity of the shadow arrivals has not been accounted for.

Orbit splitting. The early timefronts 33, 34 are split into multiple fronts with the same ray identifier but significantly different turning slowness; we refer to this as having different ray *orbits*. Orbit splitting is a manifestation of the triplication associated with the transition from surface reflection to refraction. The split is particularly pronounced for -34a,b with lower turning depths of 4.36 and 3.92 km, respectively. Timefront -34a is almost entirely surface reflected, whereas -34b has a significant mixed layer component. We associated -34a and -34b with the lower and central branches of the triplication (Fig. 17). Note that -34b is absent in the tilt

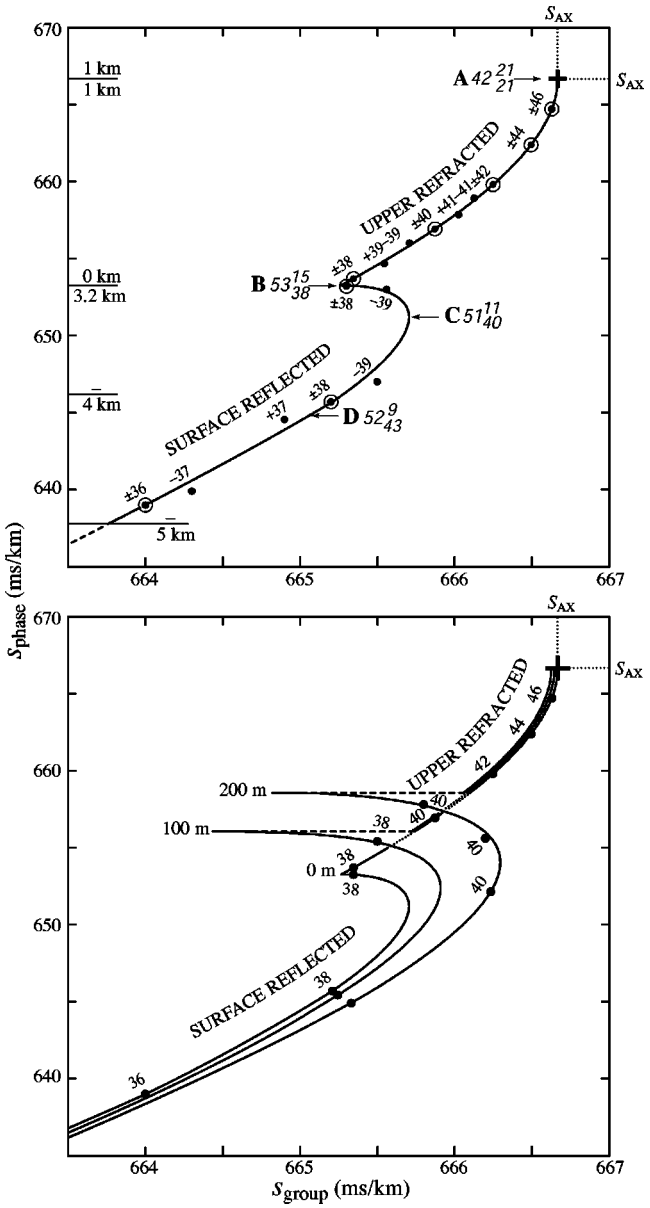

FIG. 15. Top: Dispersion for temperate profile for refracted (**A** to **B**) and surface reflected (**B** to **C** to **D**) rays. The dispersion is "normal" ($A''>0$) from **A** to **B** and from **C** to **D**, and abnormal ($A''<0$) from **B** to **C**. Numbers following **B** denote a 53 km loop length, consisting of a 15 km upper loop and 38 km lower loop, and similarly for **A**, **C**, **D**. Even identifiers ± 38, ± 40 designate upward/downward launch angles with equal numbers 19/19, 20/20 of upper/lower turning points; odd identifiers $+39$, -39 designate 20/19, 19/20 upper/lower turning points and lying slightly beneath/above the "even" dispersion curve. Some upper/lower turning depths are indicated; for an ocean depth of 5 km, the dispersion encounters bottom interaction near the lower limit (dashed). Bottom: Dispersion for 0, 100, and 200 m mixed layer depths. Refracted and surface-reflected dispersions are discontinuous for mixed layers.

ocean but clearly identified in the spice ocean.

The TPF representation (Fig. 16) exhibits $+34$ splitting and a weak and deep $+33$ arrival with 100% surface reflection and no mixed layer trapping. We detect a cluster of shallow $+33$ ray points associated with 36% surface reflection and 38% mixed layer interaction. Finally, some weak early ray arrivals are identified with -32 timefronts, 52% surface reflection and 42% mixed layer interactions.

The simulation clearly supports orbit splitting but does not convincingly demonstrate the expected triplication.

Trajectory splitting. The situation is very different for $+36$. Here we find multiple configurations of ray arrivals with no appreciable variation in the orbital turning slowness and lower turning depth. We are dealing here with a ray whose upper turning point is very near the bottom of the mixed layer, so that a tiny steepening leads to a penetration of the mixed layer and an upward refraction towards the surface. The extra loop is associated with a time delay (marked B in Fig. 16). This is more clearly seen in a traditional ray diagram (Fig. 17): ray trajectories $+36$ all turn beneath the mixed layer up to about mid-range where they encounter the sharp transition; here 20% of the rays (labeled **B**) are diverted to the surface for a single reflection. The remainder (**A**) retain their upper refracted turning points.[6] (Down-range at 800 km all $+36$ rays become surface reflected.) Some early evidence of trajectory splitting was found in a 900-km transmission in the northwest Atlantic (Brown *et al.*, 1980).

We conclude that trajectory splitting is along the s_{gr} axis (time axis), whereas orbital splitting has a major s_{ph} (depth) component. The triplication is an intrinsic feature of the SOSUS *overture* and needs to be taken into account in the acoustic interpretation of upper ocean processes. This offers interesting opportunities; for example, perturbations in travel times are of opposite sign in the central branch ($A''<0$) rather than in the other branches, suggesting *differential* times as sensitive measures of internal wave and spicy frontal activities. The perturbations are subtle and much is yet to be learned.

VI. DISCUSSION

The abrupt finale of SOFAR transmissions has been the subject of an extensive literature ever since its discovery in 1944 by Ewing and Worzel (1948); in the words of the authors (p. 4), "the end of the sound channel transmission was so sharp that it was impossible for the most unskilled observer to miss it." (We have been trying to find an objective specification ever since.) They also note (p. 8) that "a fair estimate of the distance between source and receiver can be obtained...from the over-all sound channel duration... ."

Kuperman *et al.* (2001) were the first to point out that there is also a definitive start time.[7] The physics of the overture and finale are altogether different. The former depends on the transition from refraction to surface reflection and is very sensitive to mixed layer formation and scattering; the latter depends on details of the axial sound-speed profile and is sensitive to internal wave scattering. An observation of trapping in the mixed layer goes back to Worcester (1977). A demonstration of the seasonal transition was provided by a 48-day tomography transmission in the northwest Atlantic in the fall of 1978 (Brown *et al.*, 1980). Sutton *et al.* (1997) recorded deepening of the mixed layer using acoustic modes. Simmen *et al.* (1999) have studied the arrivals associated with a 270 km transmission in April 1990 off Florida; they associate a folding of the early timefront with a complex upper ocean profile quite independent of surface reflection.

The sensitivity of the overture to upper ocean processes suggests an acoustic monitoring of seasonal (and other time)

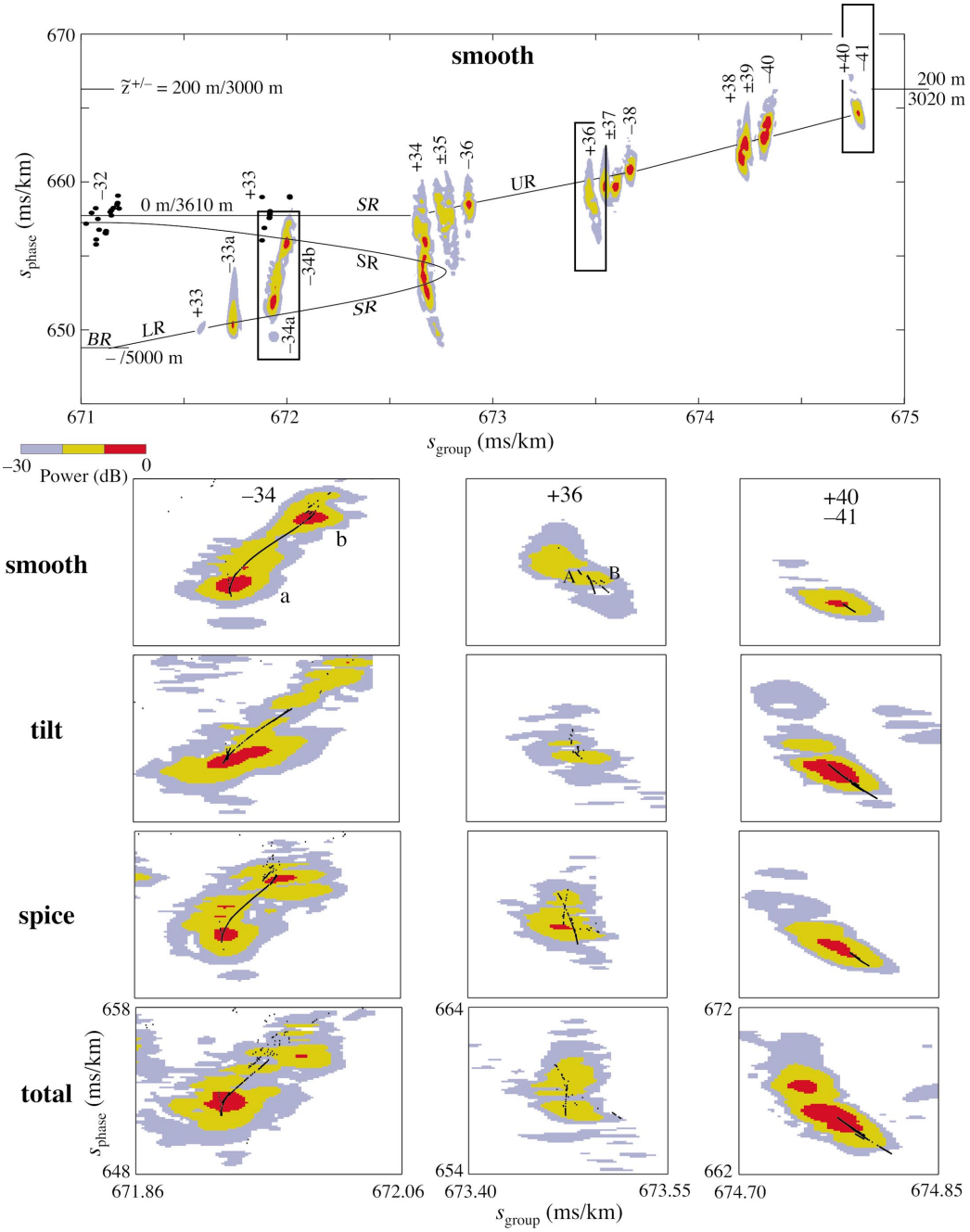

FIG. 16. Dispersion in slowness space, corresponding to $\tau, \tilde{z}^{\pm}$ space. In the lower ocean the turning depth varies from $\tilde{z}^{-}=5000$ to 3000 m, as indicated in the upper ocean from about $\tilde{z}^{+}=200$ m downward to the surface. Acoustic power (color contours) and ray arrivals (dots) define the dispersion relation, with a triplication at the transition from upper refracted (UR) to surface reflected (SR) arrivals. The three rectangles (expanded in the lower three columns) illustrate the cases of orbital splitting, trajectory splitting, and diffracted arrivals (see text).

variability of upper ocean dynamics. The problem is to determine the temporal variability of a measured mean state. (Seismologists are not so fortunate; they are confined to an invariable and unaccessible mean state.). A thin, wind-stirred layer caps much of the ocean area during winter and spring. The layer is remarkably uniform in density, with fractional differences between top and bottom of order 10^{-5}. At the same time it is populated with spice fronts across which the speed of sound changes abruptly by 10^{-3} parts. Photosynthesis in the mixed layer plays a major role in the biological productivity of the entire ocean environment. This flimsy surface film (typically 100 m out of 5000 m) puts its peculiar signature upon the acoustic transmission within the entire water column, offering the opportunity of ''viewing'' the important near-surface processes in the quiet of the deep ocean.

The standard procedure has been to place the source on the axis; this offers the entire record, from overture to finale. For the study of the early surface-interacting arrivals one can place the source at great depth, as we have in this paper. The deep ocean offers a benign environment of near-uniform temperatures and weak currents; a bottom-moored source permits short cables with small watch circles. Depth perturbations associated with orbit changes are more easily de-

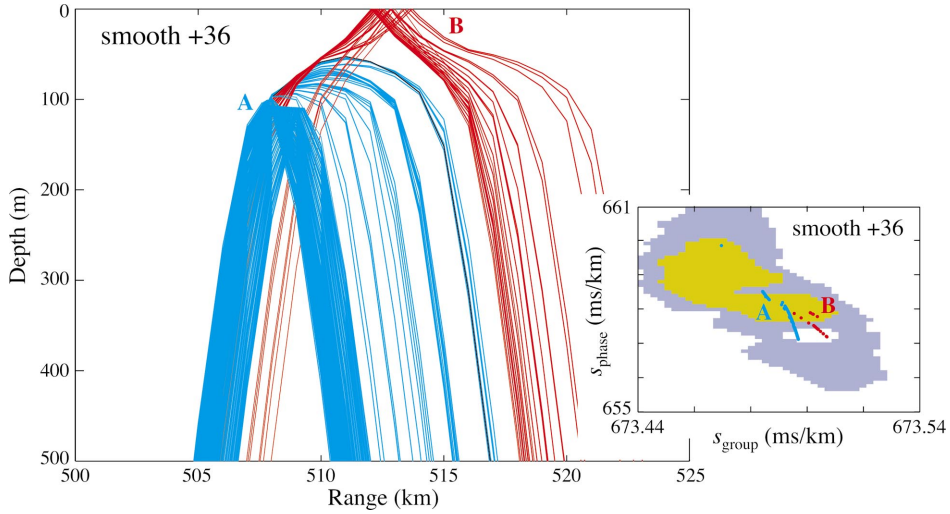

FIG. 17. Ray trajectories +36 all turn beneath the mixed layer up to mid-range, where they encounter a sharp transition: ray bundle **A** continues to turn beneath the surface, whereas **B** becomes surface reflected. The bundles are associated with two ray clusters in the dispersion (inset), an enlargement of the +36 panel in Fig. 16.

tected in the abyssal ocean; vertical displacements are inversely proportional to

$$dC/dz \approx C_A \gamma_a (N^2 - N_{AX}^2)/N_{AX}^2 \tag{14}$$

or roughly in the ratio $(N_{\text{axis}}/N_{\text{surface}})^2 = 10$ to 100 between bottom and top.

In this paper we had to rely on a *computed* sound intensity field transmitted through a *measured* sound-speed field. Plans for a 2004 experiment provide for coordinated measurements of both fields, with emphasis on the lower caustic. There is of course nothing new in monitoring upper ocean events at conjugate depths. It has been the basis of submarine detection for half a century.

ACKNOWLEDGMENTS

This paper is based largely on the application of the parabolic equation method, which was introduced into acoustics by Fred Tappert (Hardin and Tappert, 1973; Tappert, 1977). We acknowledge his influence here as well as on many previous occasions. (Tappert died while this paper was in preparation.) P. Worcester, W. Kuperman, and J. Colosi have made helpful suggestions. B. Betts and A. Santos helped prepare the manuscript. M.D. is supported by ONR Grant Nos. N00014-97-1-0258 and N00014-03-1-0182. W.M. holds the Secretary of the Navy Chair in Oceanography and is supported by ONR Grant No. N00014-03-1-0613. DLR is supported through NSF Grant Nos. OCE98-19521 and OCE00-02598.

APPENDIX: TEMPERATE PROFILE WITH SURFACE MIXED LAYER

We follow the notation in MMW 2.17 modified to include mixed layers and surface reflection. The slowness profile consists of a temperate sound channel with axis at depth $h_{SC} = 1$ km capped by an adiabatic mixed layer of thickness h_{ML} (Fig. 18). The temperate profile exhibits the up/down asymmetry of the measured profile (left panels of Fig. 10), and approaches the adiabatic gradient

$$dS/dz = S\gamma_a, \quad \gamma_a = 0.0114 \ \text{km}^{-1} \tag{A1}$$

at great depth.

The total action variable has three components:

$$A(\tilde{S}) = A_{SC}^{+} + A_{SC}^{-} + A_{ML}, \tag{A2}$$

where

$$A_{SC}^{\pm}(\tilde{S}) = S_{AX} h_{SC} \Gamma [a(1 - f_a^{\pm})\tilde{\phi}^2 \pm b(1 - f_b^{\pm})\tilde{\phi}^3 + c(1 - f_c^{\pm})\tilde{\phi}^4] \tag{A3}$$

for the upper/lower sound channel, with

$$\tilde{\phi}(\tilde{S}) = \Gamma^{-1}\sqrt{1 - (\tilde{S}/S_{AX})^2} = \Gamma^{-1}\sin\theta_{AX}, \quad \Gamma = \sqrt{\gamma_a h_{SC}}, \tag{A4}$$

$$a = \frac{\pi}{2\sqrt{2}}, \quad b = -\frac{2}{9}, \quad c = \frac{\pi}{48\sqrt{2}}. \tag{A5}$$

In the lower sound channel $f_{a,b,c}^{-} = 0$. In the upper sound channel

$$f_a^{+}(\sigma_{SC}) = (2\sigma_{SC} - \sin 2\sigma_{SC})/\pi,$$
$$f_b^{+}(\sigma_{SC}) = \sin^3 \sigma_{SC}, \tag{A6}$$
$$f_c^{+}(\sigma_{SC}) = (4\sigma_{SC} - \sin 4\sigma_{SC})/2\pi,$$

$$\sigma_{SC}(\tilde{S}, S_{ML}) = \sin^{-1}\left(\frac{S_{ML}^2 - \tilde{S}^2}{S_{AX}^2 - \tilde{S}^2}\right)^{1/2}, \tag{A7}$$

$$\tilde{S} < S_{ML} = 0, \quad \tilde{S} > S_{ML}$$

with

$$S_{ML} = S_{SU}(1 - \gamma_a h_{ML}) \tag{A8}$$

designating the slowness at the *bottom* of the mixed layer, S_{SU} being the surface slowness. For the rays with a refracted upper turning point, $\tilde{S} > S_{ML}$ hence $\sigma_{SC} = 0$ and $f_{a,b,c}^{+} = 0$; we return to the previous case of pure refraction. For the case $S_{ML} = S_{AX}$, $\sigma = 1/2\pi$ and $f_{a,b,c}^{+} = 1$: there is no upper loop.

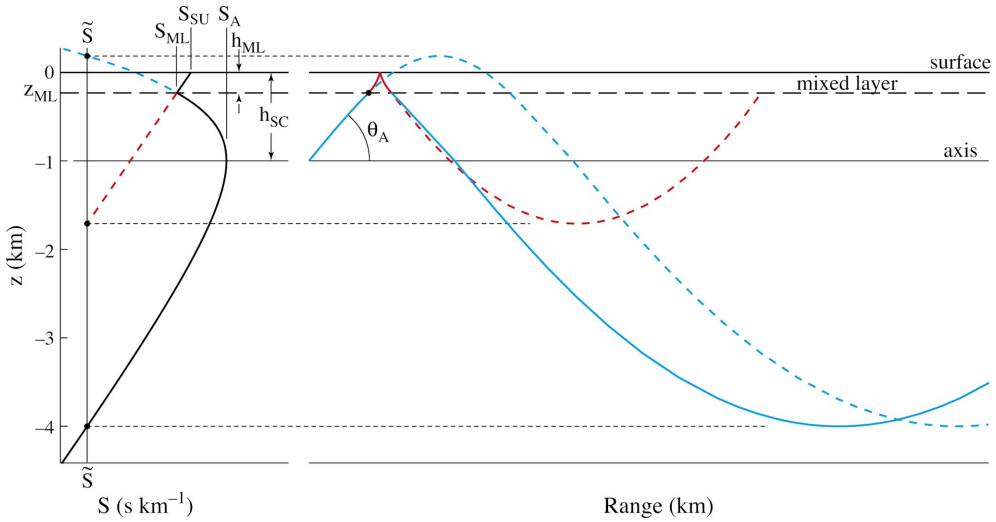

FIG. 18. Canonical sound-speed profile with adiabatic surface mixed layer. The upward refracted surface-reflected ray (blue–red–blue, solid) is drawn for a lower turning depth of 4 km with slowness $\tilde{S}$. The downward refracted ray through an upward extension of the canonical profile into the mixed layer and across the surface (blue, dashed) turns again at $\tilde{S}$, and so does the upward refracted ray through a downward extension of the adiabatic mixed layer (red, dashed).

For the case $\tilde{S}<S_{ML}$ there is a fractional upper loop within the sound channel (Fig. 18) and this is accommodated by "fractional action" as determined by $0<f^{+}_{a,b,c}<1$. The upper turning point lies above the surface; the turning slowness is determined by an upward extension of $S_{SC}(z)$ or a downward extension of $S_{ML}(z)$ as shown in Fig. 18.

For the mixed layer (MWW, 103–106)

$$A_{ML}=\frac{2}{3}\gamma_a^{-1}S_{SU}\frac{S_{SU}^2-\tilde{S}^2}{S_{SU}^2}(1-\sin^3\sigma_{ML}),$$
$$\sin\sigma_{ML}(\tilde{S},S_{ML})=\sqrt{\frac{S_{ML}^2-\tilde{S}^2}{S_{SU}^2-\tilde{S}^2}} \tag{A9}$$

for $\tilde{S}<S_{ML}$ and $A_{ML}=0$ otherwise. For a thinning mixed layer $h_{ML}\to 0$ we have $S_{ML}\to S_{SU}$ and $A_{ML}\to 0$; surface reflection is accommodated by $f^{+}_{a,b,c}(\sigma_{SC}(\tilde{S},S_{SU}))$ for $\tilde{S}<S_{SU}$.

[1]"Conjugate" refers to depths of equal sound-speed above and beneath the axis of minimum sound-speed.
[2]Spice ($\mu\pi\alpha\chi\alpha\rho\iota\kappa o$ in Greek) is denoted by μ.
[3]Usually denoted by $R=-1/n$.
[4]For Munk, Worcester, and Wunsch (1995).
[5]An even earlier timefront, +33, is detected by the turning point filter (Fig. 16).
[6]This may account for the puzzling structure of the +36 timefront (Fig. 12). The smooth timefront shows densely packed rays (**A**) but no contoured intensity between 1500 and 3000 m (the reverse holds above 1500 m). Near the turning point between 3300 and 3800 m there are both rays (**B**) and contoured intensity, the usual situation. We suspect that the anomalous occurrence of a dense ray configuration with no PE intensity is because ray theory misses the diffraction effects involved with the turning of acoustic energy near an interface. Note that the pattern is altered in the presence of scattering.
[7]The existence of both start and end times permits the estimate of range from a single station; Kuperman *et al.* (2001) attained an astounding precision of 100 km for a 3500-km transmission. A simple rule of thumb follows from the structure of ray arrivals (MWW, p. 48): the interval between ray arrivals is independent of range, but the number of ray arrivals increases linearly with range. Referring to the total record in Fig. 12, a single receiver at 200-m (or 3 km) depth receives five major pulses at roughly 1-s intervals (each pulse consists of multiple subpulses). We have $r=n^{+}R^{+}+n^{-}R^{-}$ where $n^{\pm}$ is the number of upper/lower loops of range $R^{\pm}$, respectively. For the case of an equal number of upper and lower loops, $r=nR$ where $n=n^{+}=n^{-}$ is the number of double-loops and $R=R^{+}+R^{-}$ is the double-loop range. The sound-speed profile at the receiver is consistent with $R_1=60$ km and $R_2=53$ km for the lengths of the ray double-loops with turning points at the surface and 200 m, respectively. From $r=n_1R_1=n_2R_2$ it follows that $r=(n_2-n_1)\Delta$, $\Delta=(R_2^{-1}-R_1^{-1})^{-1}=454$ km. There are two major pulses for each double-loop arrival, and we estimate $r=5/2\,454=1135$ km. The estimates can be refined by a subsequent matched filter analysis. The above procedure assumes a source beneath 200 m.

Brekhovskikh, L., and Lysanov, Y. (**1982**). *Fundamentals in Ocean Acoustics* (Springer-Verlag, Berlin).
Brown, M. G., Munk, W. H., Spiesberger, J. L., and Worcester, P. F. (**1980**). "Long-range acoustics in the northwest Atlantic," J. Geophys. Res. **85**, 2699–2703.
Collins, M. D. (**1989**). "A higher-order parabolic equation method for wave propagation in an ocean overlying an elastic bottom," J. Acoust. Soc. Am. **86**, 1459–1464.
Colosi, J. A., Flatté, S. M., and Bracher, C. (**1994**). "Internal-wave effects on 1000 km oceanic acoustic pulse propagation: Simulation and comparison with experiment," J. Acoust. Soc. Am. **96**, 452–468.
Colosi, J. A., the ATOC Group: Scheer, E., Flatté, S. M., Cornuelle, B. D., Dzieciuch, M. A., Munk, W. H., Worcester, P. F., Howe, B. M., Mercer, J. A., Spindel, R. C., Metzger, K., Birdsall, T. G., and Baggeroer, A. B. (**1999**). "Comparison of measured and predicted acoustic fluctuations for a 3250-km propagation experiment in the eastern North Pacific," J. Acoust. Soc. Am. **105**, 3202–3218.
Dushaw, B. D., Howe, B. M., Mercer, J. A., and Spindel, R. C. (**1999**). "Multimega-meter Range Acoustic Data Obtained by Bottom-Mounted Hydrophone Arrays for Measurement of Ocean Temperature," IEEE J. Ocean. Eng. **24**, 202–214.
Dzieciuch, M. (**1993**). "Numerical solution of the acoustic wave equation using Chebyshev polynomials with application to global acoustics," Proceedings of the IEEE Oceans '93 (IEEE, Piscataway, NJ), Vol. 1, pp. 267–271.
Dzieciuch, M., Worcester, P., and Munk, W. (**2001**). "Turning point filters: Analysis of sound propagation on a gyre-scale," J. Acoust. Soc. Am. **110**, 135–149.
Ewart, T. E. (**1980**). "A numerical simulation of the effect of oceanic fine-structure on acoustic transmission," J. Acoust. Soc. Am. **67**, 496–503.
Ewart, T. E., Irish, J. D., and Olsen, L. O. (**1977**). "The MATE experiment, a preliminary report," Internal Report (University of Washington, Applied Physics Laboratory).

Ewing, M., and Worzel, J. L. (**1948**). ''Long-range sond transmission,'' Geol. Soc. Am. Memoir **27**, 1–35.
Ferrari, R., and Rudnick, D. (**2000**). ''Thermohaline variability in the upper ocean,'' J. Geophys. Res. **105**, 16857–16883.
Flattè, S. M., Dashen, R., Munk, W., Watson, K., and Zachariasen, F. (**1979**). *Sound Transmission Through a Fluctuating Ocean* (Cambridge U.P., Cambridge).
Garrett, C. J. R., and Munk, W. H. (**1971**). ''Internal waves in the presence of finestructure,'' J. Phys. Oceanogr. **1**, 196–202.
Hardin, R. H., and Tappert, F. D. (**1973**). ''Applications of the split-step Fourier method to the numerical solution of nonlinear and variable coefficient wave equations,'' SIAM Rev. **15**, 423.
Kuperman, W. A., D'Spain, G. L., and Heaney, K. D. (**2001**). ''Long range source localization from single hydrophone spectrograms,'' J. Acoust. Soc. Am. **109**, 1935–1943.
Levine, M. D., and Irish, J. D. (**1981**). ''A statistical description of temperature in the presence of internal waves,'' J. Phys. Oceanogr. **11**, 676–691.
Levine, M. D., and Irish, J. D. (**1986**). ''Simultaneous spatial and temporal measurements of the internal wave field during MATE,'' J. Geophys. Res. **91**, 9709–9719.
Levitus, S. (**1994**). *World Ocean Atlas, Vol. 4 Temperature*, NOAA Atlas NESDIS No. 4 (NOAA, Washington, DC).
Levitus, S., Burgett, R., and Boyer, T. (**1994**). *World Ocean Atlas, Vol. 3 Salinity*, NOAA Atlas NESDIS No. 3 (NOAA, Washington, DC).
Munk, W. (**1981**). ''Internal Waves and small-scale processes,'' in *Evolution of Physical Oceanography—Scientific Surveys in Honor of Henry Stommel*, edited by B. Warren and C. Wunsch (MIT, Boston), pp. 264–291.
Munk, W., Worcester, P., and Wunsch, C. (**1995**). *Ocean Acoustic Tomography* (Cambridge U.P., Cambridge). To be designated MWW.
Munk, W. H., and Wunsch, C. (**1979**). ''Ocean acoustic tomography: a scheme for large scale monitoring,'' Deep-Sea Res., Part A **26**, 123–161.
Munk, W. H., and Zachariasen, F. (**1976**). ''Sound propagation through a fluctuating stratified ocean: Theory and Observation,'' J. Acoust. Soc. Am. **59**, 818–838.
Rudnick, D. L., and Ferrari, R. (**1999**). ''Compensation of horizontal temperature and salinity gradients in the ocean mixed layer,'' Science **283**, 526–529.
Rudnick, D. L., and Martin, J. P. (**2002**). ''On the horizontal density ratio in the upper ocean,'' Dyn. Atmos. Oceans **36**, 3–21.
Schmitt, R. W. (**1981**). ''Form of the temperature-salinity relationship in the central water: Evidence for double-diffusive mixing,'' J. Phys. Oceanogr. **11**, 1015–1026.
Schmitt, R. W. (**1994**). ''Double diffusion in oceanography,'' Annu. Rev. Fluid Mech. **26**, 255–285.
Simmen, J. A., Flatté, S. M., DeFerrari, H. A., Nguyen, H., and Williams, N. J. (**1999**). ''Near-caustic behavior in a 270-km acoustical experiment,'' J. Acoust. Soc. Am. **105**, 3231–3244.
Stommel, H. (**1993**). ''A conjectural mechanism for determining the thermohaline structure of the oceanic mixed layer,'' J. Phys. Oceanogr. **23**, 142–158.
Sutton, P. J., Morawitz, W., Worcester, P., and Cornuelle, B. (**1997**). ''Temperature evolution of the upper ocean in the Greenland Sea January to March 1989,'' J. Geophys. Res. **102**(C13), 27861–27874.
Tappert, F. D. (**1977**). ''The parabolic approximation method,'' in *Wave Propagation and Underwater Acoustics*, edited by J. Keller and J. Papadakis (Springer-Verlag, Berlin), pp. 224–287.
Worcester, P. F. (**1977**). ''Reciprocal acoustic transmissions in a mid-ocean environment,'' J. Acoust. Soc. Am. **62**, 895–905.
Wunsch, C. (**1987**). ''Acoustic tomography by Hamiltonian methods including the adiabatic approximation,'' Rev. Geophys. **25**, 41–53.
Young, W. R. (**1994**). ''The subinertial mixed layer approximation,'' J. Phys. Oceanogr. **24**, 1812–1826.
Yuan, X., and Talley, L. D. (**1992**). ''Shallow salinity minima in the North Pacific,'' J. Phys. Oceanogr. **22**, 1302–1316.